ELIFAN, an algorithm for the estimation of cloud cover from sky imagers

Marie LOTHON[1], Paul BARNÉOUD[1], Omar GABELLA[1], Fabienne LOHOU[1], Solène DERRIEN[1], Sylvain RONDI[2], Marjolaine CHIRIACO[3], Sophie BASTIN[3], Jean-Charles DUPONT[4], Martial HAEFFELIN[5], Jordi BADOSA[6], Nicolas PASCAL[7], and Nadège MONTOUX[8]

[1]Laboratoire d'Aérologie, Université de Toulouse, CNRS, UPS, France
[2]Direction Académique Hautes-Pyrénées, Tarbes, France; formerly Laboratoire d'Astrophysique, Toulouse-Tarbes, France
[3]LATMOS/IPSL, UVSQ Université Paris-Saclay, Sorbonne Université, CNRS, Guyancourt, France
[4]Institut Pierre-Simon Laplace, École Polytechnique, UVSQ, Université Paris-Saclay, 91128 Palaiseau, France
[5]Institut Pierre-Simon Laplace, École Polytechnique, CNRS, Université Paris-Saclay, 91128 Palaiseau, France
[6]LMD, IPSL, École Polytechnique, Université Paris-Saclay, ENS PSL Research University, Sorbonne Université, CNRS, 91128 Palaiseau France
[7]ICARE, Lilles, France
[8]Université Clermont Auvergne, CNRS, LaMP, F-63000 Clermont-Ferrand

Correspondence to: Marie LOTHON (marie.lothon@aero.obs-mip.fr)

Abstract.

In the context of a network of sky cameras installed on atmospheric multi-instrumented sites, we present an algorithm named ELIFAN which aims at estimating the cloud cover amount from full sky visible daytime images with a common principle and procedure. ELIFAN was initially developped for a self-made full sky image system presented in this article, and adapted to a set of other systems in the network. It is based on red over blue ratio thresholding for the distinction of cloudy and cloud-free pixels of the image, and on the use of a cloud-free sky library, without taking account of aerosol loading. Both an absolute (without use of cloud-free reference image) and a differential (based on a cloud-free reference image) red/blue ratio thresholding are used.

An evaluation of the algorithm based on a one-year long series of images shows that the proposed algorithm is very convincing for most of the images, with about 97% of relevance in the process, outside the sunrise and sunset transitions. During those latter periods though, ELIFAN has large difficulties to appropriately process the image, due to a large difference of color composition and a potential confusion between cloud-free and cloudy sky at that time. This issue also impacts the library of cloud-free images. Beside this, the library also reveals some limitations during daytime, with the possible presence of very small and/or thin clouds. However, the latter have only a small impact on the cloud cover estimate.

The two thresholding methodologies, the absolute and the differential red/blue ratio thresholding processes, agree very well with departure usually below 8%, except in sunrise/sunset periods and in some specific conditions. The use of the cloud-free image library gives generally better results than the absolute process. Especially, it better detects the thin cirrus clouds. But the absolute thresholding process turns out to be better sometimes, for example in some cases where the sun is hidden by a cloud.

Keywords: Sky imager, Cloud cover, Cloud fraction, Algorithm, Image processing, Instrumented Sites, ACTRIS-FR

1 Introduction

Due to their crucial role in weather and climate, clouds are the focus of many observation systems all over the world. Sky imagers are naturally used as simple devices for visible sky monitoring: They give a very useful qualitative information of the state of the sky and of the type of clouds. But they can also fulfill quantitative parameters, after a process of the image that is
either based on the texture of the image, or on the {Red, Green, Blue} color composition of the image. Historically, some of the first systems were developed for military purposes, especially for the detection of cloud free line of sight (Johnson and Hering, 1987). But soon, their applications were extended to meteorology, climate and solar energy. Ghonima et al. (2012) and Shields et al. (2013) give rich and interesting reviews of the sky imager systems and their applications. Several algorithms have now been proposed, which enable to retrieve an estimation of cloud cover (e. g. Long and DeLuisi (1998), Li et al. (2011),
Ghonima et al. (2012), Martinis et al. (2013), Silva and Echer (2013), Cazorla et al. (2015), Kim et al. (2016), Krinitskiy and Sinitsyn (2016)) or solar irradiance (Pfister et al. (2003), Chu et al. (2014), Chauvin et al. (2015), Kurtz and Kleissl (2017)), to classify the type of observed clouds (e. g. Heinle et al. (2010), Kazantzidis et al. (2012), Xia et al. (2015), Gan et al. (2017)), or to track them (Peng et al. (2015), Cheng (2017), Richardson et al. (2017)). Sky imagers have also been specifically used for the detection of cirrus (Yang et al., 2012) or thin clouds (Li et al., 2012), and contrail studies (Schumann et al., 2013).
Furthermore, one can also estimate the cloud base height (Allmen and Kegelmeyer (1996), Kassianov et al. (2005), Nguyen and Kleissl (2014)) by using a pair of sky cameras.

Those systems are now commonly deployed in the vicinity of solar farms for the intra-hour or now-casting of solar irradiance, and during atmospheric field experiments or on permanent observatories, for the cloud cover and cloud type monitoring.

Within the ACTRIS-FR [1] French research infrastructure, several instrumented permanent sites have coordinated their actions
for the observation of the atmosphere, and attempt to homogenize their instrumental, data process, and data dissemination practises, for a larger and more consistent multi-parameter data use of the international research community. In this context, a common sky imager algorithm has been developped, called ELIFAN, in order to retrieve in a similar way the cloud fraction from all the sky cameras of the different sites. It is now used on three ACTRIS-FR sites, and in progress on three other sites. ELIFAN is based on red over blue ratio (here after RBR) thresholding for the distinction of cloudy and cloud-free pixels of
the image, and on the use of a cloud-free sky library. This article aims at presenting ELIFAN algorithm principle, strength, limitations and perspectives.

In section 2, we present the sky cameras used in the ACTRIS-FR infrastructure, with more details on a self-made sky imager developed at one of the instrumented sites, and on which ELIFAN was originally based. In section 3, ELIFAN algorithm is explained in details. In section 4, an evaluation of ELIFAN highlights its main strengths and limitations. We make concluding
remarks in the last section, with perspectives of evolution of the algorithm and further discussion.

---

[1]ACTRIS-FR is the French component of the European Aerosol, Cloud and Trace Gases Research Infrastructure (ACTRIS), http://cache.media.enseignementsup-recherche.gouv.fr/file/Infrastructures_de_recherche/70/3/Brochure_Infrastructures_2018_948703.pdf

2 Sky Imager systems used

2.1 The Sky Imager systems of ACTRIS-FR Instrumented Sites

There are five important multi-instrumented sites which participate to the French infrastructurue ACTRIS-FR, and are spread over the French territory:

- P2OA (Pyrenean Platform for the Observation of the Atmosphere[2]), in the Pyrénées, near the Spanish border, in Southwest France, with two sites: one at Pic du Midi summit (42.94°N, 0.143°E) and the other close to Lannemezan, at the 'Centre de Recherches Atmosphériques' (43.13°N, 0.366°E),

- SIRTA ('Site Instrumental de Recherche par Télédétection Atmosphérique', Haeffelin et al. (2005)), at Palaiseau, south of Paris (48.72°N, 2.21°E),

- CO-PDD ('Cézeaux –Opme- Puy de Dôme'[3]) in center of France, with 3 sites: one at the Puy de Dôme summit (1465 m, 45.77°N, 2.96°E), one at Opme (680 m, 45.71°N, 3.09°E) and one at the Cézeaux University site (410 m, 45.76°N, 3.11° E)

- OHP ('Observatoire de Haute Provence'[4]) in the Provence region, in Southeast France (43.93°N, 5.71°E),

- OPAR ('Observatoire de Physique de l'Atmosphère de la Réunion'[5]) at the Reunion Island (21.08°N, 55.38°E).

All have a sky camera for the cloud monitoring, but different systems have been historically used: TSI (Total Sky Imager) (used at SIRTA, from 23/10/2008 to 24/06/2015), ASI (All Sky Imager) from EKO (used at SIRTA, CO-PDD and P2OA mountain site), Alcor System (used at OPAR), and self-made instruments (RAPACE, used at P2OA plain site, and another one at OHP).

Table 1 summarizes the systems used at 3 observatories, for which the sky images are currently processed for the cloud cover
20
retrieval.

Table 1. List of sky imager systems within the ACTRIS-FR infrastructure and their characteristics. The list here only consider the systems for which the images are processed by ELIFAN for cloud cover retrieval.

Site	Sky imager system	Solar mask	Image size	Time interval	Start year	Comment
P2OA	RAPACE	no	2048 x 1536	5 min	2006	at plain site
P2OA	EKO - SRF02	no	2272 x 1704	5 min	2017	at mountain site
SIRTA	TSI - 440	yes	640 x 480	1 min	2008	peri-urban site (former system)
SIRTA	EKO - SRF02	no	1024 x 768	2 min	2014	peri-urban site (current system)
CO-PDD	EKO - SRF02	no	1024 x 768	1 min	2015	at plain site

[2]http://p2oa.aero.obs-mip.fr/
[3]http://www.opgc.univ-bpclermont.fr/SO/mesures/
[4]http://www.obs-hp.fr/welcome.shtml
[5]http://lacy.univ-reunion.fr/observations/observatoire-du-maido-opar/

Initially, the image processing algorithm was developped and profoundly evalutated on RAPACE system images. But it was subsequently adapted for the other commercial systems, in order to realize a common data process within ACTRIS-FR sky imager network.

In the following subsection, we describe in more details the RAPACE self-made system that is at the origin of the ELIFAN algorithm development, and which will be considered for the illustrations of further sections.

2.2 RAPACE system

There are several self-made systems presented in the litterature that show that this is often a quite satisfactory option when trying to acquire good quality images at significantly lower cost than commercial systems. The developers then also design their own specific data process, depending on their objectives.

Shields et al. (2013) gives a historical and long-experienced based overview of the development and use of the Whole Sky Imager (WSI) first deployed in 1984 (Johnson et al., 1989), later improved into the day/night whole sky imager (D/N) WSI (first deployed in 1992, Shields et al., 1993) at the University of California, San Diego, USA. The WSI used a charge injection device (CID) solid-state imager and a fisheye-lens. The D/N WSI is based on Photometrics slow scan charge coupled device (CCD) camera and a fisheye-lens. It is capable of detecting cloudy and cloud free sky in starlight, moonlight and daytime (by use of near infrared over blue ratio).

Most of the systems developed in the last decade are similarly based on a digital camera coupled with an upward looking fisheye-lens (e. g. Souza-Echer et al., 2006; Seiz et al., 2007; J. and Sabburg, J. and Sabburg; Jayadevan et al., 2015). Cazorla et al. (2008) have used a CCD camera for the purpose of cloud cover estimation and characterisation. The system captures multispectral image every 5 min. Kazantzidis et al. (2012) have made a whole sky imaging system based on a commercial digital camera with a fisheye-lens and a hemispheric dome, for the automatic estimation of total cloud coverage and classification. Chu et al. (2014) has proposed an automatic smart adaptative cloud identification (SACI) system for sky imagery and solar irradiance forecast, which uses an off-the-shelf fisheye objective. Urquhart et al. (2015) have developed a high dynamic range (HDR) camera system capable of providing a full sky multispectral image at radiometric resolution, every 1.3 s.

An alternative design, instead of using a fisheye-lens, uses a spherical miror and a downward looking camera fixed above. Such systems were also historically developed in the late 1970s or early 1980s, like that mentioned in Benech et al. (1980). This type of design is used in several recent developments (e. g. Pfister et al., 2003; Long et al., 2006; Mantelli Neto et al., 2010; Chow et al., 2011).

The instrument used at P2OA plain site, called RAPACE ('Récepteur Automatique Pour l'Acquisition du Ciel Entier') was made in December 2006 at low cost, based on the first type of design, and similar to Kazantzidis et al. (2012), in the purpose of taking automatic and regular whole sky images. RAPACE System is composed of:

- a A510 CANON camera, remotely controllable,

- a Nikon FC-E9 fisheye objective, for full sky image

- a waterproof box, for protection of the camera outside,

- – a square board support, to put the camera at the right height into the box,

- – a Plexiglas dome, to protect the fisheye objective from hail, animals, and other sources of damage,

- – a thermostatted heating wire, to limit condensation and frost inside the dome,

- – a control computer,

5   – Power Shot Remote software (from Breeze Systems), for remote control of the camera.

A picture of RAPACE is shown in Fig. 1, on the roof of the P2OA plain site laboratory building. Exemples of images are shown in Fig. 2.

It has now been running since December 2006 with no significant interruption, and turned out to be a very robust system, with high quality 3.2 M pixels images taken every 15 min until February 2017 and every 5 min (during daytime, 15 min during 10   nighttime) since then.

Assuming that the main fragility would lie in the mechanical constraint endured during (i) the successive opening and closing of the digital camera objective, and (ii) focusing, we have blocked the objective in opened position, and also fixed the focus after focusing to infinity. This seemed to help a lot in the system endurance, as RAPACE has run for 12.5 years now with the same original digital camera and fisheye objective. Only the Plexiglas dome has been replaced a couple of times due to hail 15   damage, and the USB extension wires have been improved along the time.

Figure 1. The RAPACE sky imager system developed at P2OA instrumented site. We can see the fisheye-lens at the center, the Plexiglas dome and the thermostatted heating wire in spiral around the fisheye.

In the purpose of using a common and centralised data process to retrieve the cloud cover from the images of all the sky cameras available at the instrumented sites of ACTRIS-FR, an algorithm has been developed. It is now operationnally running at AERIS (Data and Services for the atmosphere) data center for the images of all the EKO systems listed in Tab. 1, and of RAPACE. This algorithm is presented in details in the next section.
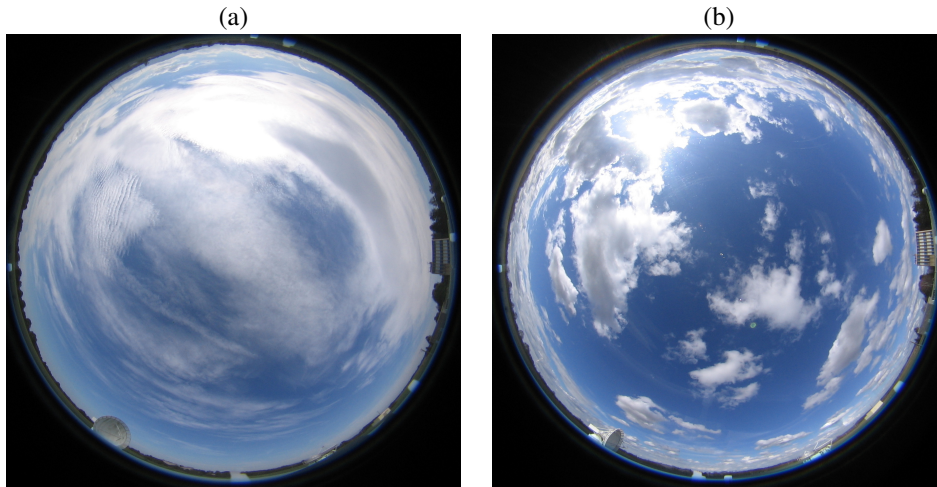
Figure 2. Two examples of RAPACE full sky images. (a) Cirrus clouds on 2 October 2007, (b) Cumulus clouds on 20 February 2006. East direction is on the right side of the image, North at the bottom.

3 ELIFAN algorithm

3.1 Background on the retrieval of cloud cover from a visible sky camera

They are several ways to detect clouds and estimate the cloud cover percentage from a visible full sky image. Table 2 summaries the different methodologies found in the litterature. Most of the algorithms lean on the colour information of the image pixels, but there are also techniques based on the texture of the image. Combining both increase the retrieval capacity, and especially gives more possibility for cloud types identification.

Within the first category, one simple and though quite efficient way to proceed is based on the use of fixed thresholds on the RBR (Shields et al. (1990), Long and DeLuisi (1998), Long et al. (2006)). This methodology is based on the fact that a cloud-free sky is characterised by pixels with larger contribution of blue relative to the two other colours, while clouds have more homogeneous relative contributions (closer to white or gray). The methodology can be sophisticated with combination of RBR and GBR (Green over Blue ratio) (Kim et al., 2016), or the use of saturation (Souza-Echer et al., 2006). One of the main difficulties lies in the variability of the colour of the cloud-free sky, from one day to another (for example due to variable aerosol loading and hydratation), and from one time to the other (due to variable sun elevation). The use of adaptative thresholding (Li et al. (2011), Jayadevan et al. (2015)) helps improving the results on this aspect. Another permanent challenge is due to the variability of the colour of cloud-free sky from one part of the image to the other. There is indeed heterogeneity within a totally cloud-free image, due to forward scattering and Mie scattering of aerosols. Depending on the position of the pixel relatively to the sun position, the cloud-free sky appears differently. It especially makes the circumsolar area very difficult to deal with (there is an increase whitening around the sun). To solve this issue, Ghonima et al. (2012) uses a real cloud-free sky library as a reference, composed of a set of cloud-free sky images found within a large dataset. The difference between the RBR of the

Table 2. Synthetic table of background studies of cloud cover retrieval algorithms from daytime visible sky camera.

Feature	Basic principle	Diagnostic	Reference
Colour	Thresholding	RBR	Shields et al. (1990)
Colour	Thresholding, perturbation RBR	RBR	Koehler et al. (1991)
Colour	Thresholding	RBR	Long and DeLuisi (1998, 2006)
Colour	Thresholding	RBR, GBR	Kim et al. (2016)
Colour	Thresholding	Saturation	Souza-Echer et al. (2006)
Colour	Adaptive Thresholding	normalised BRR	Li et al. (2011)
Colour	Adaptive Thresholding, contrast enhancing	normalised saturation value ratio	Jayadevan et al. (2015)
Colour	Adaptive Thresholding, Background substraction	G	Yang et al. (2015)
Colour	Cloud-free sky library, Thresholding	RBR	Ghonima et al. (2012)
Colour	Clear sky modeling, Background substraction	normalised RBR	Chauvin et al. (2015)
Colour	Clear sky modeling, Background substraction	G	Yang et al. (2016)
Colour	Clear sky modeling, Background substraction	B, G, BRR	Yabuki et al. (2014)
Colour	Adaptive filtering of Mie Scattering contribution	Grayness rate index	Krinitskiy and Sinitsyn (2016)
Colour	Colour transformation, K-means segmentation	RGB and luminosity	Blazek and Pata (2015)
Colour	Neural network	RGB	Taravat et al. (2015)
Colour	Neural network, neighborhood	R, G, B, all ratios	Cazorla et al. (2008)
Colour	Multiscale neighborhood and multiple learning	RGB, HSV, YCbCr	Cheng (2017)
Colour and Texture	Superpixel segmentation, thresholding	R-B	Liu et al. (2015)
Colour and Texture	Symetry of sky	R, B	Roman et al. (2017)
Colour and Texture	Neighborhood, Support Vector Machine	R, G, B, RBR, luminance	Peng et al. (2015)
Color and Texture	K-nearest neighbour	R, B	Kazantzidis et al. (2012)

processed image and the RBR of a reference cloud-free image (with similar elevation and azimuth solar angles) departs the cloudy pixels from the cloud-free pixels. Going further, recent methodologies based on background substraction take account of the clear sky spatial and temporal variability, by use of a modeled (or so-called 'virtual') clear sky (Yabuki et al. (2014), Chauvin et al. (2015), Yang et al. (2016)). Note that Koehler et al. (1991) already used a 'perturbation' ratio of RBR, relative

5 to a haze-adjusted background RBR, to optimize thin cloud detection.

Mathematical tools like neural network, K-nearest neighbour techniques, or Support Vector Machine (SVM) are also used for cloud detection, based on the RGB composition and luminosity (Blazek and Pata (2015), Taravat et al. (2015), Cheng (2017)), and on the image texture (Cazorla et al. (2008), Kazantzidis et al. (2012), Liu et al. (2015), Peng et al. (2015)). The combination of both allowed Kazantzidis et al. (2012) to distinguish seven types of clouds, in addition to estimating cloud

10 cover amount. Roman et al. (2017) interestingly uses the fact that an image of totally clear sky is symmetric.

Finally, there is of course a gain in combining instruments. Ceilometers and sky imagers are very complementary in this prospect, as the ceilometer adds the cloud base height information above the sky camera system (Chu et al. (2014), Roman et al. (2017)), which can allow to access to cloud speed motion (Wang et al., 2016). Pyranometers are also naturally considered in such instrumental synergy (Peng et al. (2015), Wang and Kleissl (2016)).

15 **3.2 Principle and methodology of ELIFAN algorithm**

Initially developed in 2013, ELIFAN algorithm aims at estimating the cloud cover percentage during daytime, based on a visible image. At that time, only RAPACE system at P2OA site and the TSI-440 system of SIRTA site were used within

the network of instrumented sites. An algorithm that could be used for both cameras, despite their differences, needed to be developed. ELIFAN is basically inspired by Ghonima et al. (2012), with the use of the RBR as the driving diagnostic to depart cloudy and cloud-free pixels by thresholding, and of a reference cloud-free sky library. Considering the literature overviewed before, ELIFAN's innovation is limited. One originality of ELIFAN though, is that it applies both an absolute and a differential thresholding processes independently. Each of them has advantages and drawbacks, but both are complementary.

3.2.1 The different steps along the process

For a given image to be processed, the different steps are the followings:

– Step 1: The image is cropped in order to remove the obstacles at horizon and the circumferential part of the image that is too distorted and cannot be properly interpreted. The cropped area is fixed, and corresponds to an aperture angle of 143° centered toward zenith. Figure 3 shows an example of a raw RAPACE image (26 February 2014 at 1300 UTC) and the corresponding cropped selection (step 1). Only the pixels located into the cropped image (i. e. inside the black circle in figure 3a) are processed.

– Step 2: A Solar mask is applied, and other masks if needed (e. g. for TSI camera, which has a sun mask arm). The solar mask is positioned based on the solar zenith and azimuth angles, which are calculated with the algorithm given by Reda and Andreas (2003), as a function of the localisation of the site, the date and the time. The coordinates of the sun in the cropped image, I_s and J_s, are then calculated with the solar angles, and taking account of the deformation due to the fisheye-lens:

$$\begin{cases} I_s = Int(A - B\sin(\alpha/2)\cos\theta) \\ J_s = Int(A - B\sin(\alpha/2)\sin\theta) \end{cases} \tag{1}$$

where θ is the solar azimuth angle (from North toward the East), α is the solar zenith angle, and A and B are adjusted according to the camera. The diameter of the sun mask is a compromise between loosing some processed pixels, and increasing the error due to circumsolar area. The sun mask diameter here is about 3 times the sun disk diameter. The sun mask represents 10% of the cropped processed image, when it is entirely included in the cropped image.

– Step 3 (see section 3.2.2): With a combination of criteria applied on the global probability density function (pdf) of the image RBR, a primary phase evaluates whether the image is totally cloudy, totally free of cloud or partly cloudy:

– A totally cloudy image is associated with 100% cloud cover;

– A totally cloud-free image is sent to the cloud-free sky library, and associated with a 0% cloud cover;

– A partly cloudy image continues the process with the following step.

– Step 4 (see section 3.2.3): As a secondary phase, all images considered as partly cloudy image during the previous step 3 are processed, with a pixel by pixel point of view. For this, the algorithm searches for a reference cloud-free sky image within a library, with the sun at same azimut and same elevation, $\pm 1°$, as the considered image.

   – If there is no reference image, the image is processed with absolute RBR threshold process

   – If there is a reference image, the image is processed with both the absolute RBR threshold process and the differential RBR threshold process. If there are several reference images available, the sky with the least turbidity is chosen as a reference, based on the RBR pdf.

Cloud cover estimate is given by the percentage of cloudy pixels / uncertain pixels / cloud-free pixels.
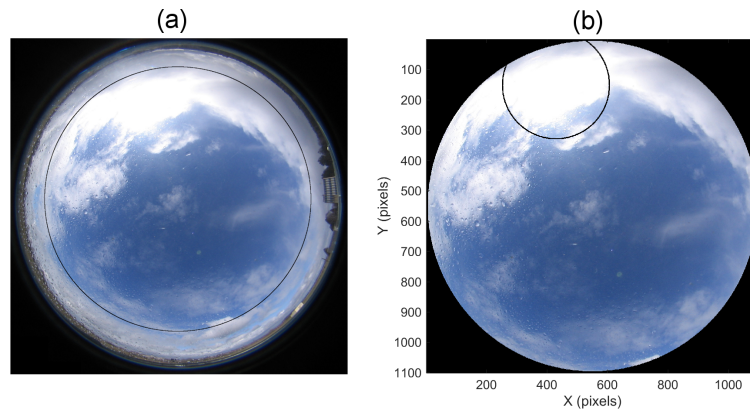
Figure 3. (a) Initial image 26.02.2014 at 1300 UTC. (b) Corresponding cropped image (Step 1 of the process). In (a), the black circles indicates the contour of the cropped image shown in (b), outside which the pixels are not processed. In (b), the black circle indicates the contour of the sun mask, within which the pixels are not processed.

A scheme of the pathway followed by the image and summarizing those steps is drawn in Fig. 4, and steps 3 and 4 mentioned above are explained and illustrated in more details in the following subsections.
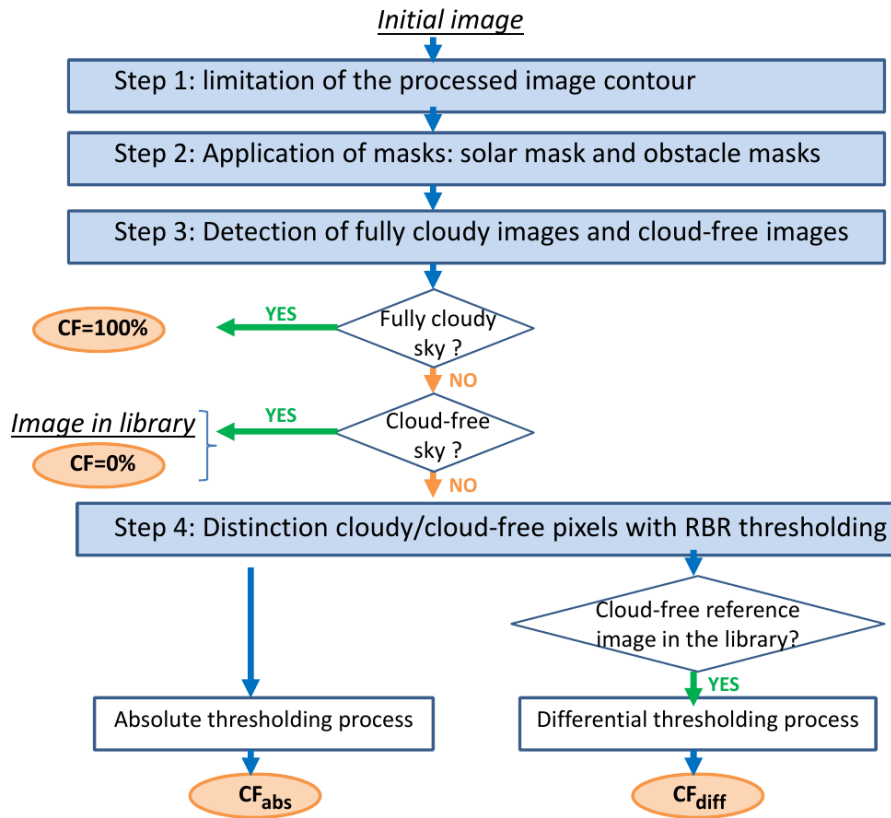
Figure 4. Organigram of the various steps followed along the image processing. CF_{abs} is the cloud fraction deduced from the absolute thresholding process, and CF_{diff} the cloud fraction deduced from the differential thresholding process.

3.2.2 Step 3: Detection of cloud-free sky and fully cloudy sky images
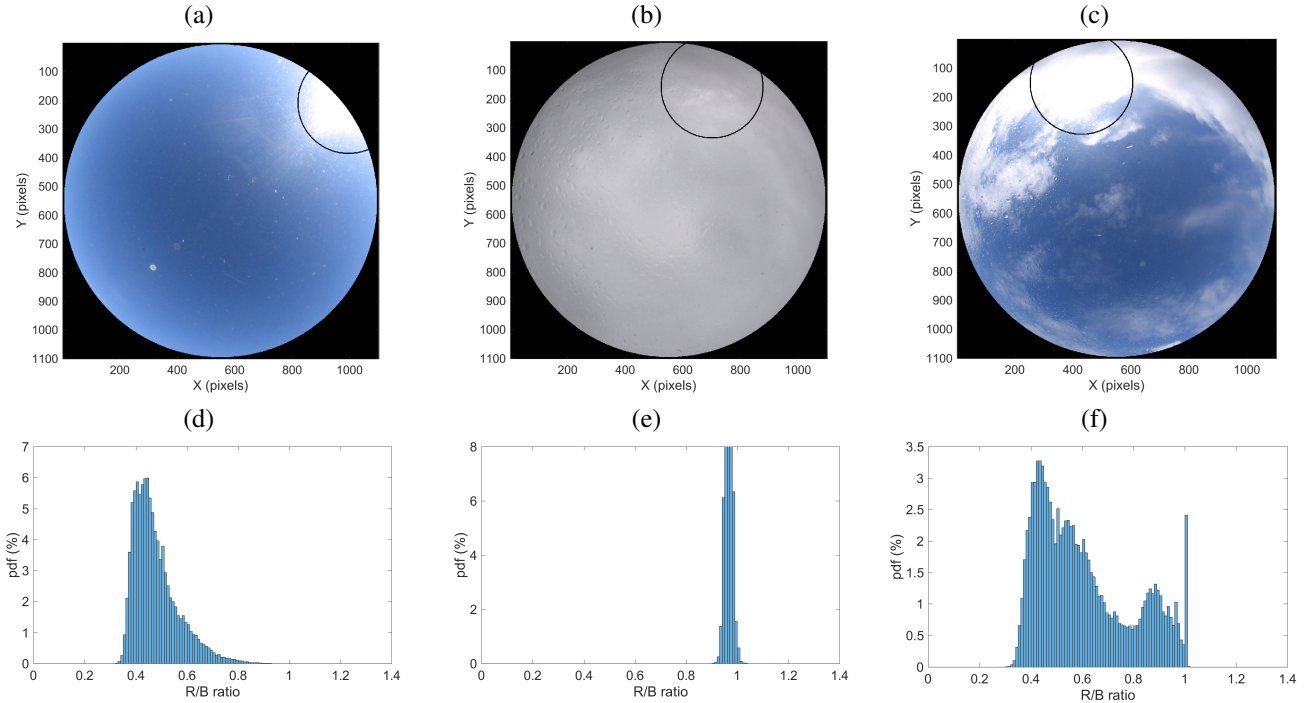
Figure 5. Cropped images of (a) 17.02.2014 at 0830 UTC, (b) 26.02.2014 at 1100 UTC, (c) 26.02.2014 at 1300 UTC, and (d, e, f) the corresponding pdf of the RBR respectively.

In step 3, the principle is to consider the cropped image as a whole, and detect whether it is a fully cloudy sky image, a fully cloud-free sky image, or neither of those two (i. e. a partly cloudy image). This step is based on the RBR distribution of the entire ensemble of pixels.

5   Figure 5 shows three examples: an image without cloud (Fig. 5a), a second with fully cloudy sky (Fig. 5b) and a third with partly cloudy sky (Fig. 5c, which is the same as in Fig. 3). In the first image (cloud-free sky, Fig. 5a), all the pixels have RBR < 0.75. The spread from 0.3 to 0.8 is due to the variability of the RBR with the scattering angle from zenith. Ghonima et al. (2012) have shown how the RBR in a given circular band of a cloud-free sky image also depends on the 500 nm aerosol optical depth (AOD), varying almost linearly with AOD from 0.3 to 0.6 in their analysis for AOD within [0, 0.3], for scattering (zenith)

10   angle within [0.35°-0.45°].

In the second image (fully cloudy, Fig. 5b), most of the pixels have RBR > 0.75. Thicker clouds have RBR closer to 1 (Ghonima et al., 2012).

In the third image (partly cloudy, Fig. 5c) the probability density function (pdf) of the RBR shows a bimodal distribution, corresponding to the two sets of cloud-free pixels in one hand (left side mode) and cloudy sky pixels in the other hand (right

15   side mode).

The main goal of step 3 is to detect whether the image is a fully cloudy image (CF=100%), or whether it is a cloud-free sky image, to be transfered to the library.

If the maximum of RBR over the entire image is smaller than 0.6 (case of darkened cloudy sky at sunrise or sunset) or if more than 98% of the pixels have RBR > 0.75 (like in Fig. 5b), then this image is defined as a fully cloudy image.

Otherwise, we check whether the image has less than 2.5% of the pixels with RBR > 0.75, but still a few pixels with RBR > 0.85. A cloud-free image meets this criterium, because it has most of its pixels with RBR < 0.75 (see Fig. 5a), but due to a few white pixels in the circumsolar region (around the sun mask here), there will be a few pixels with very high RBR (> 0.85).

So we then verify whether the image has some cloudy pixels, or is really cloud-free. If it meets at least 2 criteria among the following three criteria, it means that there are clouds in the image:

- More than 90% of the pixels have RBR within [0.45, 0.65];

- The maximum probability within the [0.45, 0.65] range is larger than 35% ;

- Less than 12.5% of the pixels have RBR ≤ 0.5.

Any image detected as full cloud-free image after this test (that is no cloud has been detected with the previous test) is sent to the cloud-free image library, and associated with the azimuth and solar zenith angle corresponding of the site and time of the image. That is how the reference library is progressively built.

At this point, any image which was not detected as a fully cloudy sky image, or as a cloud-free sky image, will be going through the process of step 4, for the estimate of the cloud fraction.

Note that the criteria explained above varies according to the sky camera. But they are all based on the RBR distribution over the entire set of pixels, and on the same main principle. The criteria remain the same all along the day.

3.2.3 Step 4: Distinction of cloudy and cloud-free pixels in a partly cloudy image

In step 4, the considered image, which is partly cloudy, is now considered at the pixel point of view, —i. e. processed pixel by pixel—, contrarily to step 3. It is independently submitted to both an absolute thresholding process and a differential thresholding process when a reference cloud-free image exists:

- The absolute thresholding process compares the RBR of each pixel to 2 thresholds T_{clear} and T_{cloud} (with 'clear' meaning 'cloud-free' here):

    If $RBR \leq T_{clear}$, the pixel is considered as cloud-free,

    if $RBR \geq T_{cloud}$ it is considered as 'cloudy',

    otherwise (for $T_{clear} \leq RBR \leq T_{cloud}$), the pixel is said 'uncertain'.

    For RAPACE imager, $T_{clear} = 0.75$ and $T_{cloud} = 0.85$. As an example, Long et al. (2006) used a unique threshold of 0.6.

- The differential tresholding process compares the RBR difference between the considered pixel and the corresponding pixel of a reference image, to 2 thresholds $Tdiff_{clear}$ and $Tdiff_{cloud}$:

  If $RBR - RBR_{lib} \leq Tdiff_{clear}$, the pixel is considered as cloud-free,

  if $RBR - RBR_{lib} \geq Tdiff_{cloud}$ it is considered as 'cloudy',

  otherwise (for $Tdiff_{clear} \leq RBR - RBR_{lib} \leq Tdiff_{cloud}$), the pixel is said 'uncertain'.

  For RAPACE imager, $Tdiff_{clear} = 0.2$ and $Tdiff_{cloud} = 0.3$.

Figure 6 gives an example of an image processed with both the absolute (Fig. 6 c, e, g) and the differential (Fig. 6 d, f, h) processes. The results for this example are 78% (84%) of cloudy pixels, 15% (10%) of cloud-free pixels, 7% (6%) of uncertain pixels for the absolute (resp. differential) process. The uncertain 'pixels' correspond to pixels that are difficult to define as cloud-free or cloudy. They usually correspond to thin cirrus, or to the border of a cloud. In this example, a stratocumulus cloud occupies most part of the image, but a thinner cirrus cloud above it can be seen in the lower part of the image. This thin cirrus is not defined as cloud by the absolute thresholding, but is partly identified through the uncertain pixels. However, it is entirely classified as a cloud by the differential process. Depending on the aim of an analysis, one may use one or the other result, or even utilise the difference for complementary information and detection of thin clouds.

Note that the reference image in Fig. 6b has some very thin cirrus clouds in the left (West-Southwest). This happens sometimes when the cloud is small and thin. They may have an impact of a few% in the final cloud cover estimate. (Note that they have no impact in the case shown here, due to the thresholds.) This uncertainty will be addressed further in section 4.
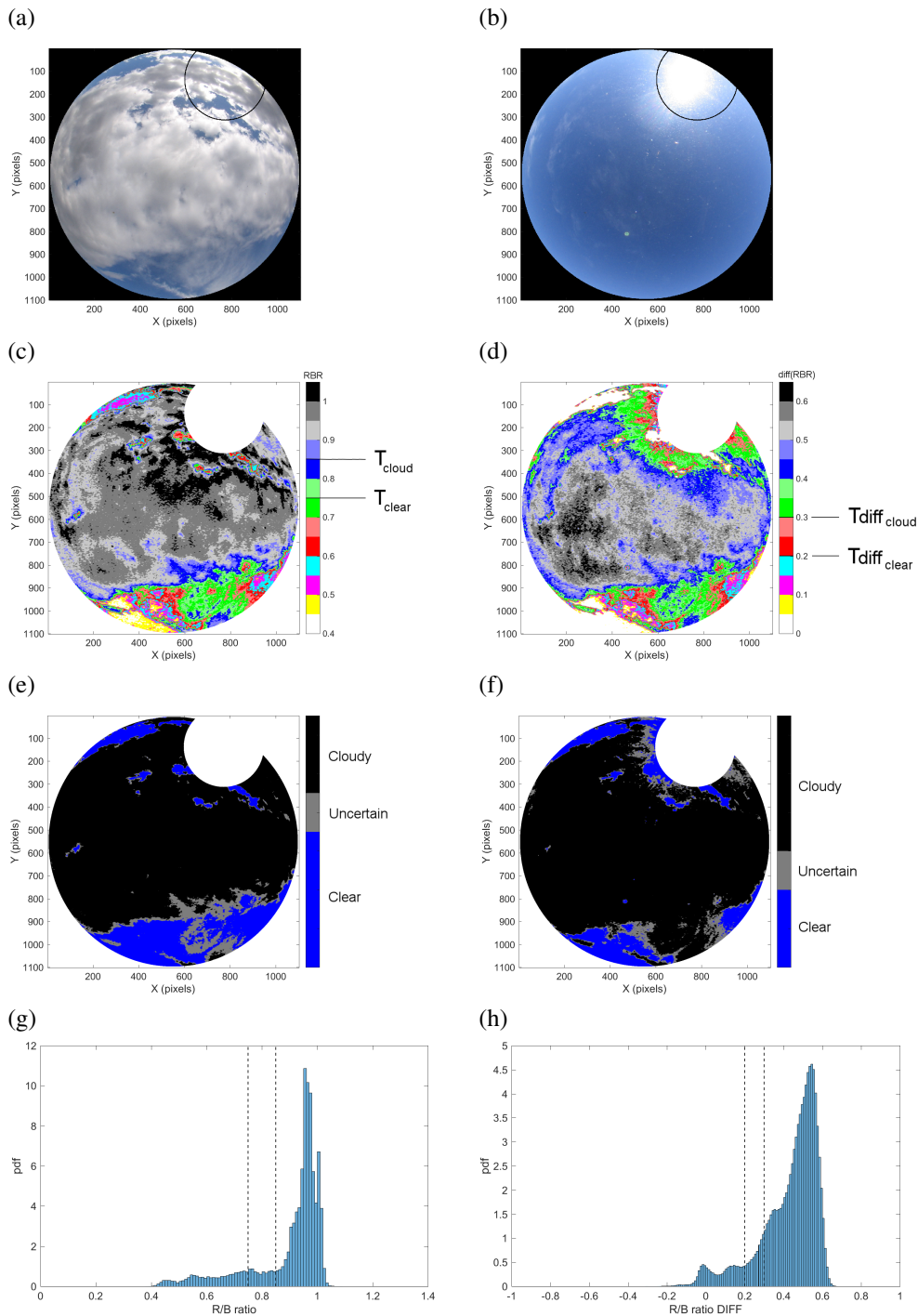
Figure 6. (a) Cropped image of 13.02.2018 10:30 UTC. (b) Cropped reference image used for differential process, 12.02.2014 10:30 UTC. (c) RBR of cropped image (a) (for absolute process). (d) RBR difference between image (a) and reference image (b) (for differential process). (e) Result of Cloudy / Cloud-free / Uncertain pixels from absolute process. (f) Result of Cloudy / Cloud-free / Uncertain pixels from differential process. (g) pdf of the RBR in initial cropped image (see (c)). (h) pdf of the RBR difference between initial cropped image and referential cropped image (see (d)). In (g), the black dashed lines correspond to the thresholds $T_{clear} = 0.75$ and $T_{cloud} = 0.85$. In (h), they correspond to the thresholds $Tdiff_{clear} = 0.2$ and $Tdiff_{cloud} = 0.3$. In (c), (d), (e), (f), 'clear' means 'cloud-free'.

3.3 Adaptation to other cameras

This algorithm has been first developed for the RAPACE imager, which had no integrated process algorithm, and then adapted to other cameras of the ACTRIS-FR instrumented sites for homogeneity of the data process within the ensemble of sites. The raw images of all sites are automatically sent to the AERIS, where ELIFAN runs and generates for each system, the corresponding libraries, the cloud cover netcdf data file, and the intermediate products (RBR, or RBR differences images like in Fig. 6 c and d, and the tricolour images of the cloudy/cloud-free/uncertain pixels distribution like in Fig. 6 e and f).

According to the systems, the image may differ in terms of geometry, color, obstructing objects,... Here are the camera-dependent aspects that need to be adjusted or defined in ELIFAN for it to run on a new full sky camera:

- The geographical coordinates and type of system (fisheye-lens and camera): they determine the solar mask position and course along time;

- Specific additional masks, needed for certain cameras;

- The image center and radius, and the radius of the cropped image;

- the RBR pdf criteria which determine whether an image is fully cloudy, fully cloud-free or partly cloudy (see step 3 above);

- RBR absolute and differential thresholding ratios, which vary from one camera to the other, and need to be optimized (see step 4 above).

The adaptation has been done for the EKO cameras listed in Tab. 1, and for the former TSI systems of SIRTA. The optimized thresholds used are indicated in Tab. 3. Those thresholds and those used in step 3 were optimized at $\pm\, 0.05$ through a sensitivity study based on one or two months of data for each camera.

Table 3. Thresholds used in step 4 for the different systems of the ACTRIS-FR instrumented sites.

Permanent site	Sky imager system	Cropped Image radius	T_{clear}	T_{cloud}	$Tdiff_{clear}$	$Tdiff_{cloud}$
P2OA	RAPACE	545	0.75	0.85	0.2	0.30
P2OA	EKO	630	0.55	0.70	0.15	0.25
SIRTA	TSI	195	0.70	0.80	0.20	0.30
SIRTA	EKO	285	0.65	0.75	0.15	0.25
CO-PDD	EKO	300	0.65	0.75	0.15	0.25

One can notice different values of thresholds within the EKO systems, with smaller thresholds for the P2OA EKO camera, relatively to the two other EKO cameras. This is likely due to the altitude of the P2OA EKO (2877 m asl), associated with less aerosols, which shifts the cloud-free image RBR pdfs toward smaller RBR values.

From the Aerosol Robotic Network (AERONET) observations (Holben et al., 1998), Ghonima et al. (2012) showed, as mentioned before, that the RBR of a TSI camera cloud-free sky image, for scattering (zenith) angle within [0.35°-0.45°], varies close to linearly with the 500 nm AOD, with a regression line that writes RBR = $0.87\, \tau_{500} + 0.4$ (where τ_{500} is the 500

nm AOD). Even if not directly applicable, this would imply that the RBR in cloud free sky may reach the threshold T_{clear} of 0.7 (used for SIRTA TSI camera) for AOD around 0.35 (and T_{cloud} of 0.8 for AOD around 0.46). Based on the ReOBS dataset (Chiriaco et al., 2018), with hourly AERONET 500 nm AOD data measured at SIRTA, we estimated to 7% (2%) the percentage of occurrence of hourly AOD larger than 0.35 (0.5) over a 10-year-long period (with 10000 values due to missing data). This is a small percentage, but not negligible. We checked that the results of ELIFAN on the corresponding images remain largely satisfying, with correct interpretation of cloud-free versus cloudy pixels, except that the mis-interpreted circumsolar region is larger than on days with smaller AOD.

A climatology made over 49 sites over the world (including the SIRTA site) by Ningombam et al. (2019), based on monthly AERONET data, shows that the climatological range of AOD observed at SIRTA is similar to that of other sites. (see Figure 3 in Ningombam et al., 2019).

This shows that the RBR thresholds used in ELIFAN for the ACTRIS-Fr cameras should be suited to a relatively large spectrum of conditions of clear sky and sites, with presence of aerosols of typical range, even if adaptative thresholds would likely be the most appropriate to manage the aerosol and haze variability. Sites like the Izaña Observatory, with frequent heavy dust events in summer (Garcia et al., 2016), and daily AOD reaching values larger than 0.7 sometimes, should be the most challenging, especially during summer.

4   Evaluation of the Algorithm, strengths and limitations

An entire year of RAPACE data (2014) has been used for ELIFAN direct evaluation, before its adaptation to other systems. Instead of considering all 15-min interval images, we considered only 1 image over 4 throughout the seasonal cycle, which resulted in a set of 4925 processed hourly images, which are thoroughly evaluated. The tricolour resulting images of the cloudy/cloud-free/uncertain spatial distribution of pixels were compared one by one to the initial images, and evaluated with human eye by a single operator (that is without quantified estimate of the actual number of successful pixels). Several aspects were systematically considered for this evaluation, focused on specific previously identified potentiel failures :

- in detecting cloud-free parts of the sky

- in detecting cloudy parts of the sky

- in detecting fully cloud-free images (that is feeding the library)

- linked with thin cirrus clouds

- in the sunrise/sunset transition periods ($\pm$ 1 hour around sunrise or sunset time)

- due to the reflection and refraction of the sun

- due to rain drops on the Plexiglas dome

The main results of this evaluation are given in a synthetic way for the entire year in Tab. 4, through a percentage of successfull processed images over the relevant ensemble of images. The absolute thresholding process is considered first for several specific aspects. The differential thresholding process is evaluated with the relevance of all images classified as cloud-free images and by checking that using the library improves the image analysis (and so the resulting cloud cover estimate).

Table 4. Eye evaluation of the performance of ELIFAN algorithm: percentage of successfull processed images in various situations or aspects, over the entire year. The total number of images of the considered ensemble is specified in each specific evaluation.

Evaluated aspect	Percentage of successfull images (%)	Total number of images in the considered ensemble	Considered ensemble
Capability of detecting clouds or cloud-free areas within the image (absolute thresholding, outside sunrise/sunset)			
cloud-free sky areas (%)	**98**	2231	All images with cloud-free areas
cloudy sky areas (%)	**97**	2715	All images with cloudy area
Capability in challenging situations (absolute thresholding)			
cirrus clouds (%)	**78**	1356	All images with cirrus clouds
sunrise/sunset (%)	**20**	783	All images within sunrise/sunset period
Relevance of the images within the library			
cloud-free image (%)	**80**	411	All images in cloud-free image library
Improvement gained with differential thresholding			
Improvement (%)	**68**	322	All images with a reference image

From this human-eye evaluation, we deduced that out off dawn and twilight times, cloudy and cloud-free parts of the sky are well identified by the absolute process, with respectively 97 and 98 % of success in the analysis (see Table 4). In other words, for 97 % of the studied images, the evaluator was generally satisfied of the absolute ELIFAN process in detecting the cloudy areas, without a quantified estimate of the successful versus failing pixels. Condensation and rain drops have generally no significant impact on the cloud cover estimate, and the number of images that are significantly impacted is about 20 over the 4925 processed images. So ELIFAN works generally very well.

However, there are clearly identified limitations: Dawn and twilight periods (corresponding to 16% of the images) are critical times, with obvious failure of the algorithm, because "cloud-free sky" is not "blue" then, and clouds are not "white or grey" (80% of failure, see Table 4). The 80% of problematic images are separated in 60% with strong failure (where the sky can be estimated totally or largely cloudy, instead of clear or weakly cloudy), and 20% of small error. This is the main weakness of the algorithm, and main prospective of progress to put the efforts on.

The cloud-free sky reference library can also be improved: 80% of the images are absolutely cloud-free. But 20% of the images in the library are found inappropriate (see Table 4). Some of them (about 1 over 6) belong to the critical dawn/twilight period. In this latter case, the failing image may be 100% cloudy rather than cloud-free. For all other 'inappropriate' reference images (17% of the reference images), only very small and/or thin clouds are present (like in Fig. 6b), so that the impact on the cloud amount estimate is small.

68% of the time, the differential process is judged better than the absolute process (see Table 4). It gives better results in detecting cloud-free areas in the circumsolar region, and also in detecting thin cirrus clouds.

The latter is illustrated in Fig. 7. In this case, quite extended thin cirrus clouds are observed in the middle of the image (Fig. 7a). Deeper cirrus clouds surround them. The absolute threshold finds a large number of uncertain pixels within the thin cirrus clouds area (Fig. 7b), while the absolute threshold process consider them as cloudy pixels (Fig. 7c). So if one wants to consider those clouds into the overall cloud cover, the differential process is doing better here. Note that the amount of

5   uncertain pixels in the absolute process interestingly gives, in this specific case, an estimate of the thin cirrus cover, relatively to the rest of the cloud cover.

One of the interest of the differential process is to deal with the circumsolar region, and not interpret the white pixels in this region as clouds, when the sky is cloud-free around the sun. This is indeed what we find. But when the sun is hidden by clouds, the reverse effect happens: cloudy pixels in this region can be interpreted as cloud-free by the differential process. An example

10 of this effect is shown in Fig. 8, where the absolute process does better in the circumsolar region than the differential process.
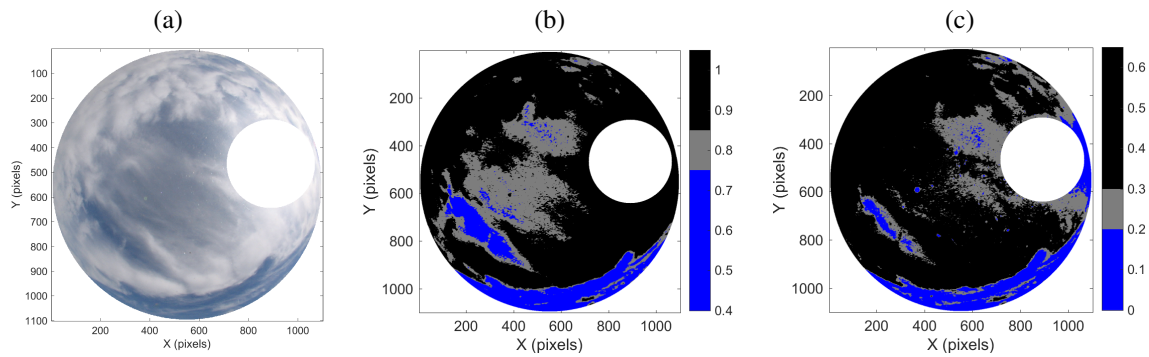
Figure 7. (a) Cropped image of 03.06.2016 at 0830 UTC. (b,c) Result of Cloudy / Cloud-free / Uncertain pixels from (b) absolute process and (c) differential process.
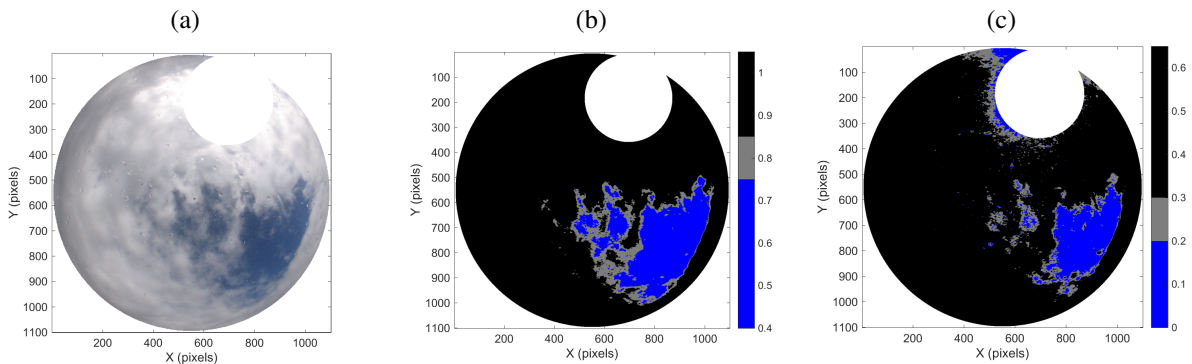
Figure 8. (a) Cropped image of 07.03.2018 at 1100 UTC. (b,c) Result of Cloudy / Cloud-free / Uncertain pixels from (b) absolute process and (c) differential process.

In addition to the previous systematic evaluation, a general statistical analysis over one year of data without decimating (more than 13000 images) was made on the departure between the cloud fraction deduced from the absolute thresholding process (CF_{abs}) and the cloud fraction deduced from the differential thresholding process (CF_{diff}). The median of the difference in percentage of cloud is 2%. The 10% and 90% quantiles of the departure are respectively at -7% and 9%. 8% of the values of $|CF_{diff} - CF_{abs}|$ are larger than 10%. And this latter number drops to 3% of the images only when we consider only the period of the day between 0900 UTC and 1500 UTC, that is when avoiding the tricky period of sunrise and sunset (this period corresponds to the following ranges of solar zenith angle: [20°-42°] for the smallest winter day, and [66°-78°] for the longest summer day). Thus, large values of the departure $|CF_{diff} - CF_{abs}|$ are associated to this transition period issue, to thin cirrus occurrence, and to other specific situations that would lead to outliers. Figure 9 shows the correlation between CF_{diff} and CF_{abs} for this same large set of images. Considering only the midday period (and so avoiding the dawn/twilight period) improves the correlation and 1-to-1 correspondence.
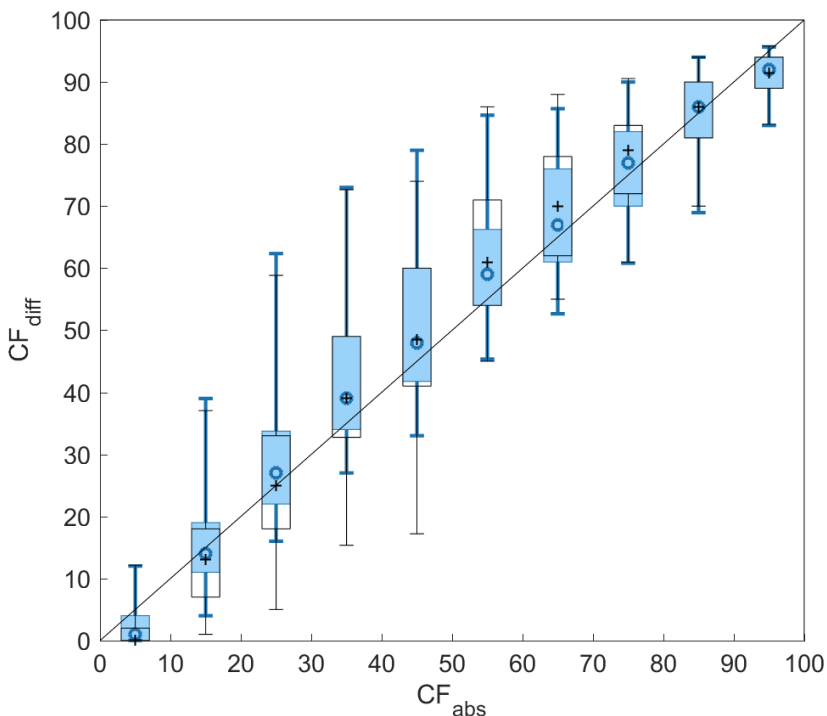
Figure 9. Comparison the cloud fraction estimates deduced from the two thresholding processes, over a set of more than 13000 images taken during one year, (black) at any time of the day and (blue) only during midday (between 0900 and 1500 UTC). CF_{diff} as a function of CF_{abs} is shown through boxplots changing with bins of values of CF_{abs}, with 10% increments. boxes represent the [25-75] percentiles interval, and the vertical lines show the limits of the 5 and 95 percentiles. The symbol into the box stands for the median.

5 Concluding remarks

From the evaluation of ELIFAN on a one-year long data evaluation, we deduced that outside the morning sunrise and sunset transitions, ELIFAN is an efficient algorithm to evaluate the cloud cover amount from a full sky camera. 97% of the daytime images with cloudy areas and 98% of images with cloud-free areas are analysed appropriately. So ELIFAN works generally very well.

However, the sunrise/sunset transition is the main weakness of the algorithm. This is where efforts should be done in the future, for improvement of ELIFAN. Specific criteria and thresholding could be applied in this time window.

Another limitation of ELIFAN is that a significant amount of library images are not perfectly cloud-free. But, outside the critical sunrise/sunset period, it usually does not strongly impact the final cloud cover amount. The differential and absolute processes remain very consistent together.

The use of the cloud-free sky library in the differential thresholding process generally improves the image process relatively to the absolute process. Especially, it better detects thin cirrus clouds. But the absolute thresholding process turns out to be sometimes better, depending on the conditions and on the reference image. It is also definitely useful for days with no reference image, or in case of casual field experiments where there is no cloud-free image library available. Moreover, the combination of both estimates may be an interesting way to access to the estimate of the thin cirrus clouds relatively to the rest of the cloud cover. But this remains to be further evaluated.

As further developement of ELIFAN, a more accurate positioning of the sun on the image will be considered, for example using the Lambert projection for the representation function that takes account of the fisheye-lens deformation, like in Crispel and Roberts (2018). In order to better take account of the presence of aerosol, the selection of the reference image in case of multiple choices could correspond to an average turbidity, rather than a minimum. Finally, adaptive thresholds method should be tested, in order to better manage the variability of aerosol and haze, on a given site, and from one site to the other.

The effort of developping a common sky-image data process for a network of sky imager has been fruitful, as now 5 cameras of the ACTRIS-FR French multi-instrumented sites have their images processed and gathered together at the same nation Data Center of AERIS (at https://actris.aeris-data.fr/data/). Three more cameras (on three other sites) should join soon.

Acknowledgements. The data of RAPACE sky imager, the ceilometer and the pyranometer used here were collected at the Pyrenean Platform for the Observation of the Atmosphere P2OA (http://p2oa.aero.obs-mip.fr). P2OA facilities and staff are funded and supported by the University Paul Sabatier, Toulouse, France, and CNRS (Centre National de la Recherche Scientifique). We thank Météo-France for the ceilometer installation at P2OA and for the data availability. We thank AERIS data infrastructure for development support and data processing, and especially the ICARE Data and Services Center. ACTRIS-FR and AERIS are supported by the French Ministry of Education and Research, CNRS, Météo-France, CEA (Centre d'Energie Atomique), INERIS (Institut national de l'environnement industriel et des risques). The developement of ELIFAN algorithm has been funded by the University Paul Sabatier of Toulouse - Observatoire Midi-Pyrénées, and by ACTRIS-FR. We thank Franck Gabarot and Alain Sarkissian for information and discusions about the sky cameras at OPAR and OHP instrumented sites. We finally thank Eric Moulin and Guylaine Canut for their fruitful inputs in the prospectives.

References

Allmen, M. C. and Kegelmeyer, W. P.: The computation of cloud-base height from paired whole-sky imaging cameras, Journal of Atmospheric and Oceanic Technology, 13, 97–113, https://doi.org/10.1175/1520-0426(1996)013<0097:tcocbh>2.0.co;2, <GotoISI>://WOS: A1996UB89900011, 1996.

5   Benech, B., Dessens, J., Charpentier, C., and Sauvageot, H.: Thermodynamic and microphysical impact of a 1000 MW heat-released source into the atmospheric environment, Proceeding of the Third WMO Scientific Conference on Weather Modification, 21-25 July 1980, 111–118, 1980.

Blazek, M. and Pata, P.: Colour transformations and K-means segmentation for automatic cloud detection, Meteorologische Zeitschrift, 24, 503–509, https://doi.org/10.1127/metz/2015/0656, <GotoISI>://WOS:000363428300004, 2015.

10   Cazorla, A., Olmo, F. J., and Alados-Arboledasl, L.: Development of a sky imager for cloud cover assessment, Journal of the Optical Society of America a-Optics Image Science and Vision, 25, 29–39, https://doi.org/10.1364/josaa.25.000029, <GotoISI>://WOS: 000252853700005, 2008.

Cazorla, A., Husillos, C., Anton, M., and Alados-Arboledas, L.: Multi-exposure adaptive threshold technique for cloud detection with sky imagers, Solar Energy, 114, 268–277, https://doi.org/10.1016/j.solener.2015.02.006, <GotoISI>://WOS:000353080700023, 2015.

15   Chauvin, R., Nou, J., Thil, S., and Grieu, S.: Modelling the clear-sky intensity distribution using a sky imager, Solar Energy, 119, 1–17, https://doi.org/10.1016/j.solener.2015.06.026, <GotoISI>://WOS:000361583300001, 2015.

Cheng, H. Y.: Cloud tracking using clusters of feature points for accurate solar irradiance nowcasting, Renewable Energy, 104, 281–289, https://doi.org/10.1016/j.renene.2016.12.023, <GotoISI>://WOS:000392779500026, 2017.

Chiriaco, M., Dupont, J. C., Bastin, S., Badosa, J., Lopez, J., Haeffelin, M., Chepfer, H., and Guzman, R.: ReOBS: a new approach
20   to synthesize long-term multi-variable dataset and application to the SIRTA supersite, Earth System Science Data, 10, 919–940, https://doi.org/10.5194/essd-10-919-2018, <GotoISI>://WOS:000432960300001, 2018.

Chow, C. W., Urquhart, B., Lave, M., Dominguez, A., Kleissl, J., Shields, J., and Washom, B.: Intra-hour forecasting with a total sky imager at the UC San Diego solar energy testbed, Solar Energy, 85, 2881–2893, https://doi.org/10.1016/j.solener.2011.08.025, <GotoISI>://WOS: 000296827400031, 2011.

25   Chu, Y. H., Pedro, H. T. C., Nonnenmacher, L., Inman, R. H., Liao, Z. Y., and Coimbra, C. F. M.: A Smart Image-Based Cloud Detection System for Intrahour Solar Irradiance Forecasts, Journal of Atmospheric and Oceanic Technology, 31, 1995–2007, https://doi.org/10.1175/jtech-d-13-00209.1, <GotoISI>://WOS:000341342100009, 2014.

Crispel, P. and Roberts, G.: All-sky photogrammetry techniques to georeference a cloud field, Atmospheric measurement techniques, 11, 593–609, https://doi.org/10.5194/amt-11-593-2018, 2018.

30   Gan, J. R., Lu, W. T., Li, Q. Y., Zhang, Z., Yang, J., Ma, Y., and Yao, W.: Cloud Type Classification of Total-Sky Images Using Duplex Norm-Bounded Sparse Coding, Ieee Journal of Selected Topics in Applied Earth Observations and Remote Sensing, 10, 3360–3372, https://doi.org/10.1109/jstars.2017.2669206, <GotoISI>://WOS:000407360200030, 2017.

Garcia, R. D., Garcia, O. E., Cuevas, E., Cachorro, V. E., Barreto, A., Guirado-Fuentes, C., Kouremeti, N., Bustos, J. J., Romero-Campos, P. M., and de Frutos, A. M.: Aerosol optical depth retrievals at the Izana Atmospheric Observatory from 1941 to 2013 by using ar-
35   tificial neural networks, Atmospheric Measurement Techniques, 9, 53–62, https://doi.org/10.5194/amt-9-53-2016, <GotoISI>://WOS: 000375610500005, 2016.

Ghonima, M. S., Urquhart, B., Chow, C. W., Shields, J. E., Cazorla, A., and Kleissl, J.: A method for cloud detection and opacity classification based on ground based sky imagery, Atmospheric Measurement Techniques, 5, 2881–2892, https://doi.org/10.5194/amt-5-2881-2012, <GotoISI>://WOS:000311804400024, 2012.

Haeffelin, M., Barthès, L., Bock, O., Boitel, C., Bony, S., Bouniol, D., Chepfer, H., Chiriaco, M., Cuesta, J., Delanoe, J., Drobinski, P., Dufresne, J.-L., Flamant, C., Grall, M., Hodzic, A., Hourdin, F., Lapouge, F., Lemaitre, Y., Mathieu, A., Morille, Y., Naud, C., Noel, V., O'Hirock, B., Pelon, J., Pietras, C., Protat, A., Romand, B., Scialom, G., , and Vautard, R.: SIRTA, a ground-based atmospheric observatory for cloud and aerosol research, Annales Geophysicae, 23, 253–275, 2005.

Heinle, A., Macke, A., and Srivastav, A.: Automatic cloud classification of whole sky images, Atmospheric Measurement Techniques, 3, 557–567, https://doi.org/10.5194/amt-3-557-2010, <GotoISI>://WOS:000279391000003, 2010.

Holben, B. N., Eck, T. F., Slutsker, I., Tanre, D., Buis, J. P., Setzer, A., Vermote, E., Reagan, J. A., Kaufman, Y. J., Nakajima, T., Lavenu, F., Jankowiak, I., and ;Smirnov, A.: AERONET - A federated instrument network and data archive for aerosol characterization, Remote Sensing of Environment, 66, 1–16, https://doi.org/10.1016/s0034-4257(98)00031-5, <GotoISI>://WOS:000076092900001, 1998.

J., C. and Sabburg, J.: Feature extraction from whole-sky ground-based images for cloud-type recognition, Journal of Atmospheric and Oceanic Technology, 25, 3–14, https://doi.org/10.1175/2007jtecha959.1, <GotoISI>://WOS:000252704300001, 2008.

Jayadevan, V. T., Rodriguez, J. J., and Cronin, A. D.: A New Contrast-Enhancing Feature for Cloud Detection in Ground-Based Sky Images, Journal of Atmospheric and Oceanic Technology, 32, 209–219, https://doi.org/10.1175/jtech-d-14-00053.1, <GotoISI>://WOS: 000349742900003, 2015.

Johnson, R. W. and Hering: Automated cloud cover measurements with a solid-state imaging system, Proceedings of the Cloud Impacts on DOD Operations and Systems, 1987 Conference, Atmospheric Sciences Division, Air Force Geophysics Laboratory, Air Force Systems Command, Hanscom Air Force Base, 59–69, 1987.

Johnson, R. W., Hering, W. S., and Shields, J. E.: Automated visibility and cloud cover measurements witha solid state imaging system, University of California, San Diego, Scripps Institution of Oceanography, Marine Physical Laboratory, SIO, 89-7, NTIS No. ADA216 906, 1989.

Kassianov, E., Long, C. N., and Christy, J.: Cloud-base-height estimation from paired ground-based hemispherical observations, Journal of Applied Meteorology, 44, 1221–1233, https://doi.org/10.1175/jam2277.1, <GotoISI>://WOS:000231701300005, 2005.

Kazantzidis, A., Tzoumanikas, P., Bais, A. F., Fotopoulos, S., and Economou, G.: Cloud detection and classification with the use of whole-sky ground-based images, Atmospheric Research, 113, 80–88, https://doi.org/10.1016/j.atmosres.2012.05.005, <GotoISI>://WOS: 000307151500008, 2012.

Kim, B. Y., Jee, J. B., Zo, I. S., and Lee, K. T.: Cloud cover retrieved from skyviewer: A validation with human observations, Asia-Pacific Journal of Atmospheric Sciences, 52, 1–10, https://doi.org/10.1007/s13143-015-0083-4, <GotoISI>://WOS:000371527300001, 2016.

Koehler, T. L., Johnson, R. W., and Shields, J. E.: Status of the whole sky imager database, Proceeding of the Cloud Impacts on DOD Operations and Systems, 1991 Conference, Phillips Laboratory, Directorate of Geophysics, Air Force Material Command, Hanscom Air Force Base, 77–80, 1991.

Krinitskiy, M. A. and Sinitsyn, A. V.: Adaptive Algorithm for Cloud Cover Estimation from All-Sky Images over the Sea, Oceanology, 56, 315–319, https://doi.org/10.1134/s0001437016020132, <GotoISI>://WOS:000379735300001, 2016.

Kurtz, B. and Kleissl, J.: Measuring diffuse, direct, and global irradiance using a sky imager, Solar Energy, 141, 311–322, https://doi.org/10.1016/j.solener.2016.11.032, <GotoISI>://WOS:000392892700030, 2017.

Li, Q. Y., Lu, W. T., and Yang, J.: A Hybrid Thresholding Algorithm for Cloud Detection on Ground-Based Color Images, Journal of Atmospheric and Oceanic Technology, 28, 1286–1296, https://doi.org/10.1175/jtech-d-11-00009.1, <GotoISI>://WOS:000296658000009, 2011.

Li, Q. Y., Lu, W. T., Yang, J., and Wang, J. Z.: Thin Cloud Detection of All-Sky Images Using Markov Random Fields, Ieee Geoscience and Remote Sensing Letters, 9, 417–421, https://doi.org/10.1109/lgrs.2011.2170953, <GotoISI>://WOS:000301236900020, 2012.

Liu, S., Zhang, L. B., Zhang, Z., Wang, C. H., and Xiao, B. H.: Automatic Cloud Detection for All-Sky Images Using Superpixel Segmentation, Ieee Geoscience and Remote Sensing Letters, 12, 354–358, https://doi.org/10.1109/lgrs.2014.2341291, <GotoISI>://WOS:000341567600028, 2015.

Long, C. N. and DeLuisi, J. J.: Development of an automated hemispheric sky imager for cloud fraction retrievals, Proceedings of the Tenth Symposium on Meteorological Observations and Instrumentation, American Meteorological Society, 171–174, 1998.

Long, C. N., Sabburg, J. M., Calbo, J., and Pages, D.: Retrieving cloud characteristics from ground-based daytime color all-sky images, Journal of Atmospheric and Oceanic Technology, 23, 633–652, https://doi.org/10.1175/jtech1875.1, <GotoISI>://WOS:000238785200001, 2006.

Mantelli Neto, S. L., von Wangenheim, A., Pereira, E. B., and Comunello, E.: The Use of Euclidean Geometric Distance on RGB Color Space for the Classification of Sky and Cloud Patterns, Journal of Atmospheric and Oceanic Technology, 27, 1504–1517, https://doi.org/10.1175/2010jtecha1353.1, <GotoISI>://WOS:000282042200006, 2010.

Martinis, C., Wilson, J., Zablowski, P., Baumgardner, J., Aballay, J. L., Garcia, B., Rastori, P., and Otero, L.: A New Method to Estimate Cloud Cover Fraction over El Leoncito Observatory from an All-Sky Imager Designed for Upper Atmosphere Studies, Publications of the Astronomical Society of the Pacific, 125, 56–67, https://doi.org/10.1086/669255, <GotoISI>://WOS:000314102800008, 2013.

Nguyen, D. and Kleissl, J.: Stereographic methods for cloud base height determination using two sky imagers, Solar Energy, 107, 495–509, https://doi.org/10.1016/j.solener.2014.05.005, <GotoISI>://WOS:000340304600047, 2014.

Ningombam, S. S., Larson, E. J. L., Dumka, U. C., Estelles, V., Campanelli, M., and Steve, C.: Long-term (1995-2018) aerosol optical depth derived using ground based AERONET and SKYNET measurements from aerosol aged-background sites, Atmos. Pollution Res., 10, 608–620, https://doi.org/10.1016/j.apr.2018.10.008, <GotoISI>://WOS:000458484300029, 2019.

Peng, Z. Z., Yu, D. T., Huang, D., Heiser, J., Yoo, S., and Kalb, P.: 3D cloud detection and tracking system for solar forecast using multiple sky imagers, Solar Energy, 118, 496–519, https://doi.org/10.1016/j.solener.2015.05.037, <GotoISI>://WOS:000359166700047, 2015.

Pfister, G., McKenzie, R. L., Liley, J. B., Thomas, A., Forgan, B. W., and Long, C. N.: Cloud coverage based on all-sky imaging and its impact on surface solar irradiance, Journal of Applied Meteorology, 42, 1421–1434, https://doi.org/10.1175/1520-0450(2003)042<1421:ccboai>2.0.co;2, <GotoISI>://WOS:000185665200006, 2003.

Reda, I. and Andreas, A.: Solar position algorithm for solar radiation application, National Renewable Energy Laboratory (NREL), Technical Report NREL/TP-560-34302, 2003.

Richardson, W., Krishnaswami, H., Vega, R., and Cervantes, M.: A Low Cost, Edge Computing, All-Sky Imager for Cloud Tracking and Intra-Hour Irradiance Forecasting, Sustainability, 9, https://doi.org/10.3390/su9040482, <GotoISI>://WOS:000402090300005, 2017.

Roman, R., Cazorla, A., Toledano, C., Olmo, F. J., Cachorro, V. E., de Frutos, A., and Alados-Arboledas, L.: Cloud cover detection combining high dynamic range sky images and ceilometer measurements, Atmospheric Research, 196, 224–236, https://doi.org/10.1016/j.atmosres.2017.06.006, <GotoISI>://WOS:000409290200019, 2017.

Schumann, U., Hempel, R., Flentje, H., Garhammer, M., Graf, K., Kox, S., Losslein, H., and Mayer, B.: Contrail study with ground-based cameras, Atmospheric Measurement Techniques, 6, 3597–3612, https://doi.org/10.5194/amt-6-3597-2013, <GotoISI>://WOS: 000330830900005, 2013.

Seiz, G., Shields, J., Feister, U., Baltsavias, E. P., and Gruen, A.: Cloud mapping with ground-based photogrammetric cameras, International Journal of Remote Sensing, 28, 2001–2032, https://doi.org/10.1080/01431160600641822, <GotoISI>://WOS:0024690330000, 2007.

Shields, J. E., Koehler, T. L., and Johnson, R. W.: Whole sky imager, Proceeding of the Cloud Impacts on DOD Operations and Systems, 1989/90 Conference, Corporation, Meetings Division, 101 Research Drive, 123–128, 1990.

Shields, J. E., Johnson, R. W., and Karr, M. E.: Automated whole sky imagers for continuous day and night cloud field assessment, Proceeding of the Cloud Impacts on DOD Operations and Systems, 1993 Conference, Phillips Laboratory, Directorate of Geophysics, Air Force Material Command, Hanscom Air Force Base, 379–384, 1993.

Shields, J. E., Karr, M. E., Johnson, R. W., and Burden, A. R.: Day/night whole sky imagers for 24-h cloud and sky assessment: history and overview, Applied Optics, 52, 1605–1616, https://doi.org/10.1364/ao.52.001605, <GotoISI>://WOS:000315894500009, 2013.

Silva, A. A. and Echer, M. P. D.: Ground-based measurements of local cloud cover, Meteorology and Atmospheric Physics, 120, 201–212, https://doi.org/10.1007/s00703-013-0245-9, <GotoISI>://WOS:000318307400008, 2013.

Souza-Echer, M. P., Pereir-A, E. B., Bins, L. S., and Andrade, M. A. R.: A simple method for the assessment of the cloud cover state in high-latitude regions by a ground-based digital camera, Journal of Atmospheric and Oceanic Technology, 23, 437–447, https://doi.org/10.1175/jtech1833.1, <GotoISI>://WOS:000236908500009, 2006.

Taravat, A., Del Frate, F., Cornaro, C., and Vergari, S.: Neural Networks and Support Vector Machine Algorithms for Automatic Cloud Classification of Whole-Sky Ground-Based Images, Ieee Geoscience and Remote Sensing Letters, 12, 666–670, https://doi.org/10.1109/lgrs.2014.2356616, <GotoISI>://WOS:000344988800046, 2015.

Urquhart, B., Kurtz, B., Dahlin, E., Ghonima, M., Shields, J. E., and Kleissl, J.: Development of a sky imaging system for short-term solar power forecasting, Atmospheric Measurement Techniques, 8, 875–890, https://doi.org/10.5194/amt-8-875-2015, <GotoISI>://WOS: 000350558300024, 2015.

Wang, G. and Kleissl, J.: Cloud base heigh estimates fro msky imagery and a network pf pyranometers, Solar Energy, 184, 594–609, https://doi.org/10.1016/j.solener.2016.02.027, <GotoISI>://WOS:000375811400019, 2016.

Wang, G., Kurtz, B., and Kleissl, J.: Cloud base height from sky imager and cloud speed sensor, Solar Energy, 131, 208–221, https://doi.org/10.1016/j.solener.2016.02.027, <GotoISI>://WOS:000375811400019, 2016.

Xia, M., Lu, W. T., Yang, J., Ma, Y., Yao, W., and Zheng, Z. C.: A hybrid method based on extreme learning machine and k-nearest neighbor for cloud classification of ground-based visible cloud image, Neurocomputing, 160, 238–249, https://doi.org/10.1016/j.neucom.2015.02.022, <GotoISI>://WOS:000354139100021, 2015.

Yabuki, M., Shiobara, M., Nishinaka, K., and Kuji, M.: Development of a cloud detection method from whole-sky color images, Polar Science, 8, 315–326, https://doi.org/10.1016/j.polar.2014.07.004, <GotoISI>://WOS:000346894800001, 2014.

Yang, J., Lu, W. T., Ma, Y., and Yao, W.: An Automated Cirrus Cloud Detection Method for a Ground-Based Cloud Image, Journal of Atmospheric and Oceanic Technology, 29, 527–537, https://doi.org/10.1175/jtech-d-11-00002.1, <GotoISI>://WOS:000303396400006, 2012.

Yang, J., Min, Q., Lu, W., Yao, W., Ma, Y., Du, J., Lu, T., and Liu, G.: An automated cloud detection method based on the green channel of total-sky visible images, Atmospheric Measurement Techniques, 8, 4671–4679, https://doi.org/10.5194/amt-8-4671-2015, <GotoISI>://WOS:000365978100007, 2015.

Yang, J., Min, Q. L., Lu, W. T., Ma, Y., Yao, W., Lu, T. S., Du, J., and Liu, G. Y.: A total sky cloud detection method using real clear sky background, Atmospheric Measurement Techniques, 9, 587–597, https://doi.org/10.5194/amt-9-587-2016, <GotoISI>://WOS: 000375612000017, 2016.